Decentralized Power Transfer Limit Calculation Method Considering Spatial and Seasonal Differences of Ambient Factors

Xueyong Jia, Xiaoming Dong, Chengfu Wang, Ming Yang, and Tianguang Lu

***Abstract*—Power transfer limit (PTL) calculation plays an important role in assessing power network capability under certain constraints of system security and stability. However, the impact of ambient factors, which is different due to variations in time and space, is ignored in traditional methods to obtain PTL, thus inducing errors. Furthermore, system operation based on traditional PTL results may increase system security risks, particularly in the case of power flow congestion under heavy loads. Therefore, this paper proposes a decentralized PTL calculation method with improved optimal power flow model, which allows for the effect of the ambient factors characterized by the balance of heat absorption and dissipation for overhead conductors. The ambient factors of overhead transmission lines and the temperature of overhead conductors are involved as independent variables and state variables, respectively. Moreover, the sequential optimization problem is decomposed into several subproblems by the optimal conditional decomposition to deal with the temporal coupling constraints, and a parallel decomposition framework is used to solve multiple subproblems in parallel. Finally, the proposed method is implemented on two test systems under varying ambient factors, demonstrating the efficiency of the proposed method and the significant impacts of spatial and seasonal differences on PTL results.**

***Index Terms*—Power transfer limit, ambient factor, spatial and seasonal difference, electro-thermal coupling, optimal condition decomposition.**

NOMENCLATURE

A. Parameters

α	Step size
α_s	Solar absorptivity
σ	Temperature coefficient of resistance
θ_s	Effective angle of incidence of solar rays
δ	Solar declination
φ	Angle between wind and axis of conductor
ω, ε_e	Hour angles relative to noon and emissivity
ε	Difference between two consecutive iterations
$\varepsilon_{\min}$	The minimum allowable convergence threshold
b_{Pi}, b_{Qi}	Active and reactive power growth directions of bus i
C_a	Solar azimuth constant
DR_x	The maximum ramp rate of generator x
D	Conductor diameter
H_e	Elevation of conductor above sea level
H_c	Solar altitude
K_s	Correction factor of solar altitude
L_a	Latitude
mC_p	Total heat capacity of conductor
N	Day of the year
N_T	Total number of time intervals
$P_l^{\max}$	The maximum active power capacity of overhead transmission line (OTL) l
P_{Li}, Q_{Li}	Active and reactive power loads of bus i
$P_{gx}^{\min}$, $P_{gx}^{\max}$	The minimum and maximum active power outputs of generator x
$Q_{gx}^{\min}$, $Q_{gx}^{\max}$	The minimum and maximum reactive power outputs of generator x
Q_s	Total solar and sky radiated heat intensity
R_{ref}	Series resistance per unit length at reference temperature of conduct T_{ref}
S_{base}, Z_{base}, I_{base}, U_{base}	System base power, base impedance, base current, and base voltage
$T_l^{\max}$	The maximum allowable operation temperature of OTL l
T_{ref}	Reference temperature of conductor
T_a, V_w	Ambient temperature and wind speed around OTLs
$V_i^{\min}$, $V_i^{\max}$	The minimum and maximum bus voltage magnitudes of bus i
X_l, L_l	Series reactance and length of OTL l
Z_a	Angle difference between solar azimuth and OTL

Manuscript received: September 8, 2024; revised: December 10, 2024; accepted: March 12, 2025. Date of CrossCheck: March 12, 2025. Date of online publication: June 5, 2025.

This work was supported by National Natural Science Foundation of China (No. U22B20102).

X. Jia, X. Dong (corresponding author), C. Wang, M. Yang, and T. Lu are with the School of Electrical Engineering, Shandong University, Jinan 250061, China (e-mail: 202034658@mail.sdu.edu.cn; dongxiaoming@sdu.edu.cn; wangcf@sdu.edu.cn; myang@sdu.edu.cn; tlu@sdu.edu.cn).

DOI: 10.35833/MPCE.2024.000997

MPCE JOURNAL OF MODERN POWER SYSTEMS AND CLEAN ENERGY

Z_l, Z_c	Azimuths of OTL and solar

B. Functions

β	Ratio of consumption time
ρ_f	Density of air
μ_f	Absolute (dynamic) viscosity of air
$E_{\max}^{PTL}$, $E_{\min}^{PTL}$	The maximum and minimum value differences between $\boldsymbol{\chi}_{D,1\text{-}4}$ and χ_T
E_{range}^{PTL}	Value difference between $E_{\max}^{PTL}$ and $E_{\min}^{PTL}$
E_r	Error of calculation results
f_i^p, f_i^q	Active and reactive power balance equations of bus i
f_l^I	Dynamic electro-thermal coupling (ETC) equation of OTL l
H^{loc}, M^{loc}	Local equality and inequality constraints
H^{comp}, M^{comp}	Complicating equality and inequality constraints
K_s	Correction factor of solar altitude
K_a	Wind direction factor
k_f	Thermal conductivity of air at T_f
N_{RE}	Number of reynolds
Q_l^{IR}, $\hat{Q}_l^{IR}$	Actual and per-unit values of Joule heat of OTL l
Q_l^c, Q_l^s, Q_l^r	Convective heat loss, heat gain from sun, and radiated heat loss of OTL l

C. Variables

$\boldsymbol{\lambda}$	Vector of load growth parameters
λ_t	Load growth parameter at time t
γ, μ, η	Lagrange multipliers for complicating constraints
τ_1, τ_2	Consumption time for centralized and decentralized methods
$\boldsymbol{\chi}_{D,i}$	Time evolution of power transfer limit (PTL) calculated by decentralized method in scenario i
χ_T	PTL calculated by traditional method in scenario 5
$\boldsymbol{\chi}_{C,i}$	Time evolution of PTL calculated by centralized method in scenario i
G_{ij}, B_{ij}	Conductance and susceptance from bus i to bus j
$\boldsymbol{P}_g$, $\boldsymbol{Q}_g$	Vectors of active and reactive power outputs of generator
P_{gx}, Q_{gx}	Active and reactive power outputs of generator x
R_l, P_l, T_l, I_l	Series resistance, active power flow, temperature, and current of OTL l
T_f	Average temperature of boundary layer
$\boldsymbol{T}$	Vector of temperature of overhead conductor
γ_s	Solar azimuth variable
$\boldsymbol{V}$, $\boldsymbol{\theta}$	Vectors of bus voltage magnitude and voltage angle
V_i, V_j	Voltage magnitudes of buses i and j

D. Indexes and Sets

i	Index of buses
S_B, S_C, S_R	Sets of buses, source area buses, and powered sink buses
x, S_G	Index and set of generators
t, S_T	Index and set of time intervals
l, S_L	Index and set of OTLs

I. INTRODUCTION

EXTREME weather events arising from global warming may directly or indirectly cause damage to power infrastructures over a wide range, potentially leading to serious power grid blackouts [1]-[3]. For example, in mid-August 2020, California, USA, experienced the most severe heat wave since 1985, with the average maximum temperature rising to nearly 40 °C. Extremely high temperature will directly lead to a surge in electricity demand and affect the transmission capacity and safe operation of overhead transmission lines (OTLs). Due to severe weather, a major transmission line upstream of the California Independent System Operator was disrupted, reducing the transmission capacity of the California-Oregon Interconnection by approximately 650 MW [4]. Similarly, on September 6, 2020, due to high temperature, a blackout of the transmission line between Oregon and California, USA caused a 900 MW power supply loss [5]. Consequently, the transmission capacity is markedly constrained under extreme weather conditions, which creates the need to study power transfer limit (PTL) considering the impacts of ambient factors.

A central issue for electricity market is to confirm the maximum power that can be safely transferred to a receiving center, termed as PTL [6]. PTL is determined by the current system operation states, constraints, power growth modes, and uncertainty factors, which significantly influence the transmission capacity [7]. The main causes of uncertainty affecting transmission capacity include generator failure, transmission line failure, load forecasting error, volatility of renewable energy, network topology information, etc. A stochastic model for evaluating transfer capability is proposed in [8], [9] with the assumption that the availability of generators and transmission lines is treated as a random variable obeying a binomial distribution, and the load fluctuation is treated as a normally distributed variable. Using the Monte Carlo method of sequential simulation to generate hourly load fluctuations and equipment unavailability samples as input, the linear optimal power flow (OPF) is used to evaluate each sample transfer capability [10]. In [11], an evaluation of interval total transfer capability with uncertain renewable energy integration is proposed to obtain the upper (optimistic) and lower (pessimistic) bounds of total transfer capacity. A new data-driven sparse polynomial chaotic extension method is proposed in [12] to estimate the probabilistic transfer capability. Considering the uncertainties and dependencies of wind power, a two-layer optimization framework is developed in [13], where transfer capability evaluation is formulated as an upper-level problem and economic dispatch is formulated as a lower-level problem. Using the upper and lower boundaries to represent the uncertainty of new energy output, a transfer capability evaluation model based on interval optimization is proposed in [14]. Reference [15] proposes an improved continuation power flow model to calculate the PTL among interconnected networks corresponding to either saddle node bifurcation or limit-induced bifurcation. Considering the existence of information barriers between regions, a decomposition coordination strategy for PTL calculation method is introduced in [16]. The above studies make significant contributions to analyzing the impact of various uncertainties on transfer capability. However, the influence of ambient factors on transfer capability requires further investigation.

Recently, many researchers have focused on studying the impact of ambient factors on power system operation, as these factors influence line resistance and temperature, thereby affecting the system operation state. Ignoring the effects of electro-thermal coupling (ETC) of OTLs may introduce analysis errors [17]. Reference [18] proposes a weather-based OPF algorithm with wind farm integration by considering the temperature-related resistance and ETC of OTLs. In [19], a photovoltaic accommodation evaluation model that integrates the temperature-dependent resistance and the ETC equation is proposed. Reference [20] proposes a linear OPF considering the impact of ETC for security-constrained unit commitment. Although the above research considers the ETC of OTLs, PTL calculation method attracts no focus. Reference [21] proposes an OTL-PTL calculation method by solving the ETC equations for the dynamic heat exchange process affected by various ambient factors. Additionally, new power flow formulations, which consider the relationship between transmission power flow and thermal balance, are derived in [22] to calculate PTL. Reference [6] proposes an improved continuation power flow (CPF) considering the ETC of OTLs for PTL calculation method. In [23], a probabilistic PTL evaluation considering dynamic line rating based on a sequential game-theoretic method is proposed. However, the above studies have several limitations. ① The electro-thermal relationship of OTLs can be expressed in two methods. References [6], [18], [19], [22], and [23] focus only on the steady-state ETC of OTLs, neglecting their dynamic thermal behavior. ② While [20] and [21] account for the dynamic thermal behavior of OTLs, incorporating dynamic ETC equations introduces a set of time-coupled nonlinear equality constraints to calculation models. Thus, these studies mainly rely on linearized dynamic ETC equations. ③ References [21] and [22] are limited to calculate the PTL of a single OTL. ④ Reference [7] cannot ensure that all constraints are satisfied, whereas [23] employs a linear OPF model that does not consider bus voltage and line temperature constraints. ⑤ The variations in ambient factors exhibit notable spatial and seasonal differences, and different ambient factors cause differences in PTL values. However, the above studies focus only on the impact of ambient factors on PTL under given conditions but overlook their spatial and seasonal differences.

To reduce the computation complexity of time-coupled constraints, researchers have proposed various decentralized methods, including the alternating direction method of multiplier (ADMM), the auxiliary problem principle (APP), etc. [24]. Among the decentralized methods, optimal conditional decomposition (OCD) can find primal and dual solutions that are assigned to each subproblem (SP) based on the Karush-Kuhn-Tucker (KKT) first-order optimality condition. The main advantage of this method is that the SP has a decentralized structure and can be processed in parallel. Additionally, it does not require parameter tuning and involves minimal information exchange [25]. In recent years, OCD has been successfully applied in different research areas of power systems, including the multi-area state estimation [26], dynamic economic dispatch [27], and microgrid operation [28]. The simulation results show that OCD is computationally efficient. However, the application of OCD to dealing with time-coupling constraints of the dynamic ETC equations in the PTL calculation problem remains an uncharted area of investigation.

To fill the above research gaps, this paper proposes a temporal decomposition method to solve the improved OPF model for PTL calculation method. The main contributions of this paper are summarized as follows.

1) An improved OPF model, which accounts for the dynamic ETC equations, is proposed to provide more accurate algorithm support for accurately calculating PTL values over a certain time horizon. Moreover, ambient factors around the OTLs are involved as variables in the PTL calculation method, and line temperature constraints are also taken into consideration.

2) The temporal decomposition method based on OCD is used to decouple the centralized PTL calculation problem into multiple SPs by handling time-coupling constraints, such as ramping and dynamic ETC constraints. Additionally, the method is implemented within a parallel decomposition framework, which can solve multiple SPs in parallel.

3) Based on meteorological data from various regions and seasons within the selected area, the case studies demonstrate the impact of ambient factors on PTL from spatial and seasonal perspectives and verify the effectiveness and scalability of the proposed decentralized PTL calculation method.

II. PTL CALCULATION MODEL CONSIDERING IMPACTS OF AMBIENT FACTORS

In [6], an ETC-CPF method is employed to calculate the PTL value λ_b. However, this method has several limitations: ① it is a static analysis method without considering dynamic behaviors, such as ambient factors; and ② it cannot ensure that all constraints remain within the feasible region. Although [6] defines PTLs as points where the thermal limit of the transmission line is reached or voltage collapse is detected, the manual determination is required for PTL value. To address these issues, this paper formulates the PTL calculation as an OPF problem over a time horizon. Figure 1 shows the comparison of PTL values calculated by CPF and OPF methods. From the initial operation point λ_0, generator output in the source area and load consumption in the sink area gradually increase. When all constraints are simultaneously satisfied, the power system reaches its PTL value λ_a. If λ continues to increase, it will violate certain constraints.

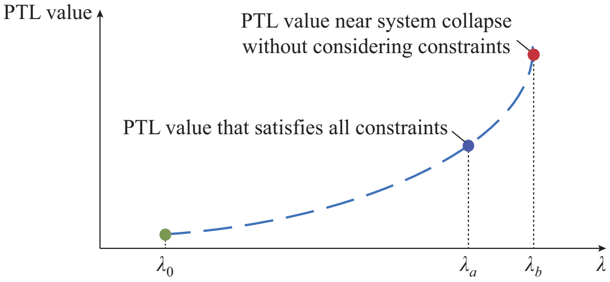

Fig. 1. Comparison of PTL values calculated by CPF and OPF methods.

The centralized PTL calculation model is described in (1)-(11). The objective of the OPF is to maximize load consumption between the initial and terminal points in the sink area, which corresponds to the PTL value. It should be noted that only static safety constraints are considered.

$$\min f(\boldsymbol{P}_g, \boldsymbol{Q}_g, \boldsymbol{V}, \boldsymbol{\theta}, \boldsymbol{T}, \boldsymbol{\lambda}) = -\sum_{t=1}^{N_T}\sum_{k\in S_R}\lambda_t b_{P,k} \tag{1}$$

s.t.

$$f_i^p(\boldsymbol{P}_{g,t}, \boldsymbol{V}_t, \boldsymbol{\theta}_t, \boldsymbol{T}_t, \lambda_t) = 0 \quad i\in S_B, t\in S_T \tag{2}$$

$$f_i^q(\boldsymbol{Q}_{g,t}, \boldsymbol{V}_t, \boldsymbol{\theta}_t, \boldsymbol{T}_t, \lambda_t) = 0 \quad i\in S_B, t\in S_T \tag{3}$$

$$f_l^I(\boldsymbol{EP}_{t-1}, \boldsymbol{EP}_t, \boldsymbol{AP}_{t-1}, \boldsymbol{AP}_t) = 0 \quad l\in S_L, t\in S_T \tag{4}$$

$$P_{gx,t-1} - DR_x \le P_{gx,t} \le DR_x + P_{gx,t-1} \quad x\in S_G, t\in S_T \tag{5}$$

$$P_{gx}^{\min} \le P_{gx,t} \le P_{gx}^{\max} \quad x\in S_G, t\in S_T \tag{6}$$

$$Q_{gx}^{\min} \le Q_{gx,t} \le Q_{gx}^{\max} \quad x\in S_G, t\in S_T \tag{7}$$

$$V_i^{\min} \le V_{i,t} \le V_i^{\max} \quad i\in S_B, t\in S_T \tag{8}$$

$$P_{l,t} \le P_l^{\max} \quad l\in S_L, t\in S_T \tag{9}$$

$$T_{l,t} \le T_l^{\max} \quad l\in S_L, t\in S_T \tag{10}$$

$$\lambda_t \ge 0 \quad t\in S_T \tag{11}$$

Equations (2) and (3) represent the active and reactive power balance constraints, respectively. Equation (4) defines the dynamic ETC equations of OTL, where $\boldsymbol{AP} = [\boldsymbol{T}_a, \boldsymbol{V}_w, \boldsymbol{\varphi}, \boldsymbol{H}_e, \boldsymbol{Q}_s]$, $\boldsymbol{EP} = [\boldsymbol{V}, \boldsymbol{\theta}, \boldsymbol{T}]$, and note that the variable in bold denotes the matrix form of the corresponding variable. Equation (5) represents the ramping constraint of generators. Equations (6) and (7) define the active and reactive output constraints of generators, respectively. Equations (8) and (9) correspond to the bus voltage and branch power constraints, respectively. Equation (10) represents the maximum operation temperature constraint of the OTLs. For the functions f_i^p and f_i^q, the detailed expressions are given as:

$$f_{i,t}^p = P_{gi,t} - P_{Li,t} - \sum_{j=1}^{n} P_{inj}(\boldsymbol{EP}_t) \quad i\in S_C, t\in S_T \tag{12}$$

$$f_{i,t}^q = Q_{gi,t} - Q_{Li,t} - \sum_{j=1}^{n} Q_{inj}(\boldsymbol{EP}_t) \quad i\in S_C, t\in S_T \tag{13}$$

$$f_{i,t}^p = P_{gi,t} - P_{Li,t} - \lambda_t b_{Pi} - \sum_{j=1}^{n} P_{inj}(\boldsymbol{EP}_t) \quad i\in S_R, t\in S_T \tag{14}$$

$$f_{i,t}^q = Q_{gi,t} - Q_{Li,t} - \lambda_t b_{Qi} - \sum_{j=1}^{n} Q_{inj}(\boldsymbol{EP}_t) \quad i\in S_R, t\in S_T \tag{15}$$

The detailed expressions for active power injection P_{inj} and reactive power injection Q_{inj} are given as:

$$P_{inj} = V_i\sum_{j=1}^{n} V_j(G_{ij}(T_{l,t})\cos\theta_{ij} + B_{ij}(T_{l,t})\sin\theta_{ij}) \tag{16}$$

$$Q_{inj} = V_i\sum_{j=1}^{n} V_j(G_{ij}(T_{l,t})\sin\theta_{ij} - B_{ij}(T_{l,t})\cos\theta_{ij}) \tag{17}$$

R_l is typically assumed to be a constant, neglecting the impact of ETC. However, in practice, the relationship between $T_{l,t}$ and R_l is approximately linear within a certain temperature range.

$$R_l(T_{l,t}) = L_l R_{ref}[1 + \sigma(T_{l,t} - T_{ref})] \tag{18}$$

G_{ij} and B_{ij} are functions of $T_{l,t}$ given as:

$$G_{ij}(T_{l,t}) = \frac{R_l(T_{l,t})}{R_l^2(T_{l,t}) + X_l^2} \tag{19}$$

$$B_{ij}(T_{l,t}) = \frac{-X_l}{R_l^2(T_{l,t}) + X_l^2} \tag{20}$$

According to [29], $T_{l,t}$ is dynamically affected by two types of heat sources. The conductor is heated by $Q_{l,t}^{IR}$ with respect to I_l. Additionally, $T_{l,t}$ is significantly affected by the heat exchange between the conductor and the ambient factors, including $Q_{l,t}^s$, $Q_{l,t}^c$, and $Q_{l,t}^r$. It is assumed that the three-phase conductors have identical structures, thermal properties, and ambient conditions. Thus, the OTLs operate at the same internal temperature, and the dynamic electro-thermal relationship of the OTL could be expressed as:

$$f_{l,t}^I = mC_p\frac{\mathrm{d}T_l}{\mathrm{d}t} - Q_{l,t}^{IR}(T_{l,t}) - Q_{l,t}^s + Q_{l,t}^c(T_{l,t}) + Q_{l,t}^r(T_{l,t}) \tag{21}$$

The detailed expressions of $Q_{l,t}^{IR}$, $Q_{l,t}^s$, $Q_{l,t}^c$, and $Q_{l,t}^r$ are given as:

1) Joule heat

$$Q_{l,t}^{IR}(T_{l,t}) = \frac{I_l^2 R_l(T_{l,t})}{L_l} \tag{22}$$

2) Heat gain from the sun

$$Q_{l,t}^s = \alpha_s D K_s Q_{s,t}\sin\theta_s \tag{23}$$

$$K_s = 1 + 1.148\times 10^{-4} H_e - 1.108\times 10^{-8} H_e^2 \tag{24}$$

$$\begin{cases}\theta_s = \arccos(\cos H_c\cos Z_a)\\ H_c = \arcsin(\cos\delta\cos\omega\cos L_a + \sin\delta\sin L_a)\end{cases} \tag{25}$$

$$Z_a = Z_c - Z_l = (C_a + \arctan\gamma_s) - Z_l \tag{26}$$

$$C_a=\begin{cases}0 & \gamma_s\geq 0, -180\leq\omega<0\\ 360 & \gamma_s<0, 0\leq\omega<180\\ 180 & \text{else}\end{cases} \tag{27}$$

$$\gamma_s=\frac{\sin\omega}{\sin L_a\cos\omega-\cos L_a\tan\delta} \tag{28}$$

$$\delta=23.46\sin\frac{(284+N)360}{365} \tag{29}$$

3) Convective heat loss

$Q^{c}_{l,t}$ is determined by comparing natural convection $Q^{cn}_{l,t}$ and forced convection $Q^{cfl}_{l,t}$ and $Q^{cfh}_{l,t}$. Specifically, $Q^{cfl}_{l,t}$ is used under low wind speed conditions, while $Q^{cfh}_{l,t}$ is used under high wind speed conditions, as shown in (30).

$$\begin{cases}Q^{c}_{l,t}=\max(Q^{cn}_{l,t}, Q^{cfl}_{l,t}, Q^{cfh}_{l,t})\\ Q^{cn}_{l,t}=3.645\rho^{0.5}_{f,t}D^{0.75}(T_{l,t}-T_{a,t})^{1.25}\\ Q^{cfl}_{l,t}=k_{f,t}K_a(1.01+1.35N^{0.52}_{RE,t})(T_{l,t}-T_{a,t})\\ Q^{cfh}_{l,t}=k_{f,t}K_a(0.754N^{0.6}_{RE,t})(T_{l,t}-T_{a,t})\end{cases} \tag{30}$$

$$N_{RE,t}=D\rho_{f,t}V_{w,t}\mu^{-1}_{f,t} \tag{31}$$

$$K_{a,t}=1.194-\cos\varphi_t+0.194\cos(2\varphi_t)+0.368\sin(3\varphi_t) \tag{32}$$

$$k_{f,t}=2.424\times10^{-2}+7.477\times10^{-5}T_{f,t}-4.407\times10^{-9}T^{2}_{f,t} \tag{33}$$

$$\rho_{f,t}=\frac{1.293-1.525\times10^{-4}H_e+6.379\times10^{-9}H^{2}_{e}}{1+0.00367T_{f,t}} \tag{34}$$

$$\mu_{f,t}=1.458\cdot10^{-6}T^{-1}_{f,t}(T_{f,t}+273)^{1.5}+383.4 \tag{35}$$

$$T_{f,t}=\frac{T_{l,t}+T_{a,t}}{2} \tag{36}$$

4) Radiated heat loss

$$Q^{r}_{l,t}(T_{l,t})=17.8D\varepsilon_e\cdot10^{-8}[(273+T_{l,t})^4-(273+T_{a,t})^4] \tag{37}$$

In the above formulations, $Q^{s}_{l,t}$, $Q^{c}_{l,t}$, and $Q^{r}_{l,t}$ are functions of ambient factors, which primarily include ambient temperature, wind speed, wind angle, light intensity, and altitude [29]. To simplify the calculation, the differential equation (21) is discretized using the improved Euler method, which can be expressed as:

$$\begin{aligned}T_{l,t+1}-T_{l,t}=&\frac{\Delta t}{2mC_p}(Q^{IR}_{l,t+1}(T_{l,t+1})+Q^{s}_{l,t+1}(t+1)-Q^{c}_{l,t+1}(T_{l,t+1})-\\ &Q^{r}_{l,t+1}(T_{l,t+1})+Q^{IR}_{l,t}(T_{l,t})+Q^{s}_{l,t}(t)-Q^{c}_{l,t}(T_{l,t})-Q^{r}_{l,t}(T_{l,t}))\end{aligned} \tag{38}$$

Throughout the entire computation process, known values are converted to per-unit values, while I_l and R_l in (21) and (22) remain as known values. Therefore, after the conversion to per-unit values, (21) and (22) can be expressed as:

$$\begin{aligned}T_{l,t+1}-T_{l,t}=\frac{\Delta t}{2mC_p}\Bigg(&\frac{S_{base}}{3}\hat{Q}^{IR}_{l}(T_{l,t+1})+Q^{s}_{l,t+1}-Q^{c}_{l,t+1}(T_{l,t+1})-\\ &Q^{r}_{l,t+1}(T_{l,t+1})+\frac{S_{base}}{3}\hat{Q}^{IR}_{l,t}(T_{l,t})+Q^{s}_{l,t}(t)-\\ &Q^{c}_{l,t}(T_{l,t})-Q^{r}_{l,t}(T_{l,t})\Bigg)\end{aligned} \tag{39}$$

$$\hat{Q}^{IR}_{l}(T_{l,t})=\frac{\hat{I}^{2}_{l}\hat{R}_l(T_{l,t})}{L_l}=\frac{3Q^{IR}_{l}(T_{l,t})}{S_{base}} \tag{40}$$

$$\hat{R}_l=\frac{R_l}{Z_{base}}=\frac{S_{base}R_l}{U^{2}_{base}} \tag{41}$$

$$\hat{I}_l=\frac{I_l}{I_{base}}=\frac{\sqrt{3}\,U_{base}I_l}{S_{base}} \tag{42}$$

Based on whether these constraints involve multiple time intervals, they are categorized as either local or complicating constraints. Equations (2), (3), and (6)-(10), which contain information only from the current time interval, are classified as local constraints. In contrast, (4) and (5), which span multiple time intervals, are classified as complicating constraints. The PTL calculation model can be compactly expressed as:

$$\min f(\boldsymbol{x}_1,\boldsymbol{x}_2,\ldots,\boldsymbol{x}_t,\ldots,\boldsymbol{x}_{N_T})=\sum_{t=1}^{N_T}f_t(\boldsymbol{x}_t) \tag{43}$$

s.t.

$$H^{loc}_{t}(\boldsymbol{x}_t)=0\quad t\in S_T \tag{44}$$

$$M^{loc}_{t}(\boldsymbol{x}_t)\leq 0\quad t\in S_T \tag{45}$$

$$H^{comp}_{t}(\boldsymbol{x}_{t-1},\boldsymbol{x}_t)=0\quad t\in S_T \tag{46}$$

$$M^{comp}_{t}(\boldsymbol{x}_{t-1},\boldsymbol{x}_t)\leq 0\quad t\in S_T \tag{47}$$

$$\boldsymbol{x}_t=[\boldsymbol{P}_{g,t}\quad \boldsymbol{Q}_{g,t}\quad \lambda_t\quad \boldsymbol{AP}_t\quad \boldsymbol{EP}_t]\quad t\in S_T \tag{48}$$

In the above formulations, (44) and (45) are local constraints. Equation (44) encompasses (2) and (3), while (45) includes (6)-(10). Conversely, (46) and (47) represent complicating constraints, where (46) corresponds to (4) and (47) corresponds to (5). The overall time horizon consists of N_T time intervals, as illustrated in Fig. 2. For the first time interval, $\boldsymbol{x}_0$ is derived from the final time interval of the previous day to ensure continuity across scheduling horizons. At the final time interval, the corresponding variables are only used to the current horizon and do not influence subsequent scheduling.

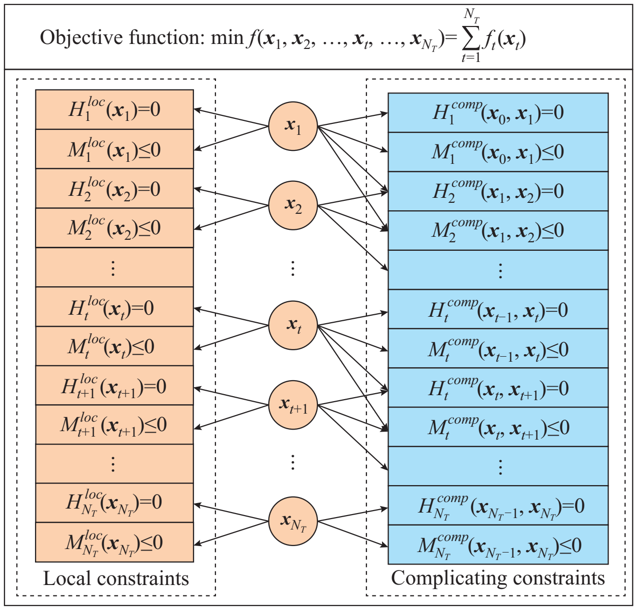

Fig. 2. Centralized scheduling with N_T time intervals.

III. TEMPORAL DECOMPOSITION STRATEGY FOR PTL CALCULATION METHOD

The centralized PTL calculation is a high-dimensional nonlinear programming problem, especially when dynamic ETC equations are considered. The number of nonlinear inequality and equality constraints significantly increases, making the problem more challenging to solve. To address this, the centralized model is decomposed into N_T low-dimensional SPs ($\mathrm{SP}_1, \mathrm{SP}_2, \ldots, \mathrm{SP}_{N_T}$) using OCD, which effectively reduces the complexity of each SP [27]. The k^{th} iteration of the SP_t is expressed as:

$$\begin{aligned}\min f_t^{(k)}(\boldsymbol{x}_t^{(k)},\bar{\boldsymbol{x}}_{t+1}^{(k-1)})=&-\lambda_t^{(k)}\sum_{i\in S_R} b_{Pi}+\bar{\gamma}_{t+1}^{(k-1)}\sum_{l=1}^{L}\Bigg[\bar{T}_{l,t+1}^{(k-1)}-T_{l,t}^{(k)}-\\&\frac{\Delta t}{2mC_p}\Bigg(\frac{S_{base}}{3}\bar{Q}_{l,t+1}^{IR}(\bar{T}_{l,t+1}^{(k-1)})+\bar{Q}_{l,t+1}^{s}-\bar{Q}_{l,t+1}^{c}(\bar{T}_{l,t+1}^{(k-1)})-\\&\bar{Q}_{l,t+1}^{r}(\bar{T}_{l,t+1}^{(k-1)})+\frac{S_{base}}{3}Q_{l,t}^{IR}(T_{l,t}^{(k)})+Q_{l,t}^{s}-Q_{l,t}^{c}(T_{l,t}^{(k)})+-Q_{l,t}^{r}(T_{l,t}^{(k)})\Bigg)\Bigg]+\\&\bar{\mu}_{t+1}^{(k-1)}\sum_{i=1}^{N}(\bar{P}_{gi,t+1}^{(k-1)}-P_{gi,t}^{(k)}-DR_i)+\bar{\eta}_{t+1}^{(k-1)}\sum_{i=1}^{N}(P_{gi,t}^{(k)}-\bar{P}_{gi,t+1}^{(k-1)}-DR_i)\end{aligned}\tag{49}$$

s.t.

$$f_l^{I}(\overline{\boldsymbol{EP}}_{t-1}^{(k-1)},\boldsymbol{EP}_t^{(k)},\boldsymbol{AP}_{t-1},\boldsymbol{AP}_t)=0\tag{50}$$

$$\bar{P}_{gi,t-1}^{(k-1)}-DR_i\le P_{gi,t}^{(k)}\le DR_i+\bar{P}_{gi,t-1}^{(k-1)}\tag{51}$$

$$(2),\ (3),\ (6)\text{-}(10)\tag{52}$$

For the k^{th} iteration of the SP_t, the complicating constraints at $t+1$ are introduced into the objective function. The electrical parameters at $t-1$ and $t+1$ are obtained from the data of the $(k-1)^{\text{th}}$ iteration. The original problem is then decomposed into N_T SPs for the k^{th} iteration. It should be noted that parameters with a bar indicate the values of the corresponding variables from the previous iteration, i.e., iteration $k-1$. Unlike the traditional Lagrange relaxation algorithm, OCD does not require designing a Lagrange multiplier update strategy. Since each SP is solved using the interior-point method (IPM) , the Lagrange multipliers for (50) and (51) are updated based on the Newton direction derived from the KKT conditions. Additionally, the local convergence of OCD has been rigorously proven in [30]. The k^{th} iteration of the SP_t can be compactly expressed as:

$$\begin{aligned}\min h_t(\boldsymbol{x}_t^{(k)},\bar{\boldsymbol{x}}_{t+1}^{(k-1)})=f_t(\boldsymbol{x}_t^{(k)})+\bar{\gamma}_{t+1}^{(k-1)}H_{t+1}^{comp}(\boldsymbol{x}_t^{(k)},\bar{\boldsymbol{x}}_{t+1}^{(k-1)})+\\ \bar{\mu}_{t+1}^{(k-1)}M_{t+1}^{comp}(\boldsymbol{x}_t^{(k)},\bar{\boldsymbol{x}}_{t+1}^{(k-1)})\end{aligned}\tag{53}$$

s.t.

$$H_t^{loc}(\boldsymbol{x}_t^{(k)})=0\tag{54}$$

$$M_t^{loc}(\boldsymbol{x}_t^{(k)})\le 0\tag{55}$$

$$H_t^{comp}(\bar{\boldsymbol{x}}_{t-1}^{(k-1)},\boldsymbol{x}_t^{(k)})=0\tag{56}$$

$$M_t^{comp}(\bar{\boldsymbol{x}}_{t-1}^{(k-1)},\boldsymbol{x}_t^{(k)})\le 0\tag{57}$$

Figure 3 illustrates the decentralized scheduling with N_T SPs.

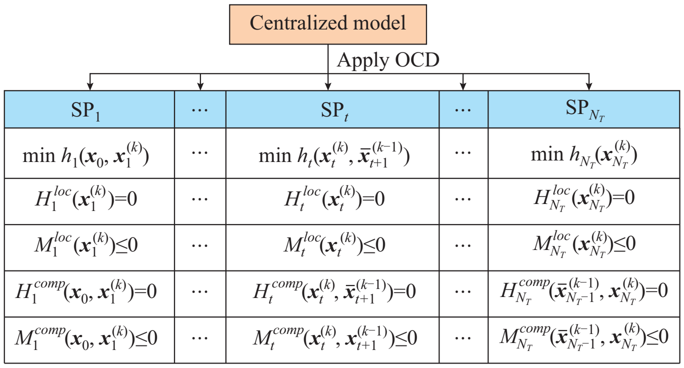

Fig. 3. Decentralized scheduling with N_T SPs.

The process of the proposed decentralized PTL calculation method is outlined in Fig. 4 [31]. $\boldsymbol{x}_{ini}=[\boldsymbol{P}_{g,ini}, \boldsymbol{Q}_{g,ini}, \boldsymbol{\lambda}_{ini}, \boldsymbol{AP}_{ini}, \boldsymbol{EP}_{ini}]$, which applies the steady-state PTL calculation method for each SP, and the detailed definitions of each variable can be found in [31].

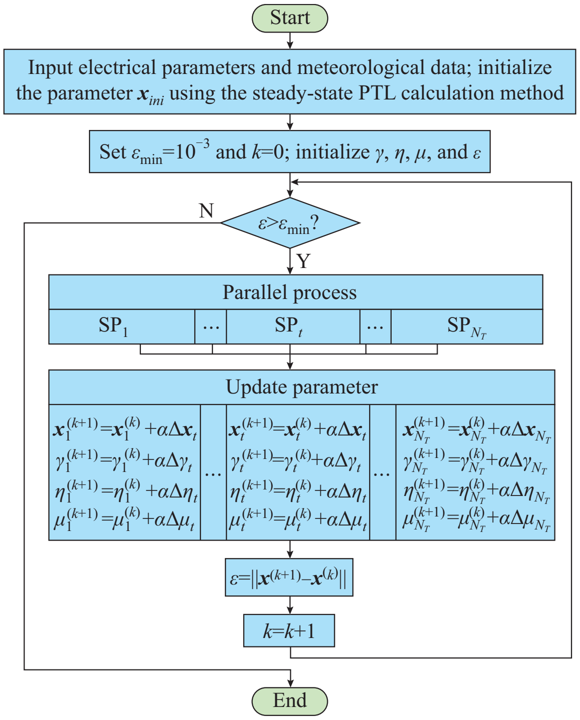

Fig. 4. Process of proposed decentralized PTL calculation method.

IV. CASE STUDY

A. Data Description

The meteorological data of the selected area from the ERA5 hourly data at single levels of the European Centre for Medium-Range Weather Forecasts (ECMWF) from 1979 to the present [32], with spatial-temporal resolutions of 1 hour and 0.25° longitude multiplying 0.25° latitude, form the foundation for the proposed PTL calculation method. Then, the selected area is divided into 18 regions. According to the geographical location of the power network structure, the ambient data around the OTLs are collected. To illustrate the influence of spatial and seasonal differences of ambient factors on the time evolution curves of PTL, calculations by the centralized and decentralized PTL calculation methods are deployed and analyzed for the following five scenarios. Scenarios 1-4 include four typical days for four seasons: spring, summer, autumn, and winter. Scenario 5 ignores the changes in ambient factors around the OTLs, and the resistance of the OTLs is equal to that of the traditional method. Moreover, the ambient data of OTLs include the ambient temperature, light intensity, wind speed, wind direction, and altitude. Supplementary Material A Fig. SA1 shows the geographical location, dominant wind direction θ_{dom}, average wind speed V_{ave}, average ambient temperature T_{ave}, and the maximum light intensity $Q_{S\max}$ of 18 regions (bus 1) for four scenarios. It should be noted that the value of N_T is set to be 96. This value can be adjusted based on specific scenarios. When N_T takes a larger value, the accuracy of the results improves, but the computation complexity grows significantly.

As shown in Fig. SA1, the elevation of region *k* is relatively higher (approximately 5000 m), compared with region *o*, which is only 34 m above the sea level. In general, V_{ave} in scenario 1 is higher than that in other scenarios, while V_{ave} in scenario 4 is the lowest. θ_{dom} often shows random uncertainty. T_{ave} in scenario 1 is higher than that in scenarios 2 and 3, and T_{ave} in scenario 4 is lower than that in scenarios 2 and 3. In addition, the maximum difference of $Q_{S\max}$ among different reference nodes is above 500 W/m^2. Through the above analysis, the difference in ambient data among regions in four seasons is considerable. Besides, [33] and [34] prove that altering ambient factors significantly impacts on the transmission characteristics of the power system. Therefore, it is worthwhile to investigate the difference in the time evolution curves of PTL in various regions under various seasons.

To describe the nonuniform spatial distribution of ambient data around OTLs, a transmission line segment model is established. Besides, if some ambient factors change considerably in a short time, the temporal resolution of ambient data will be improved by polynomial data fitting algorithm.

1) Transmission Line Segment Model

For an OTL with a long distance, if the ambient temperature of OTL only takes the average value of the first node and last node, it will introduce a certain error in calculating the PTL value. According to [35] and [36], the ambient temperature distribution between measurement sites is assumed to be linear and monotonic. Then, considering the ambient temperature changes along the OTL, virtual nodes are added to long-distance OTLs by selecting intervals based on the distance parameter d_v. The value of d_v is determined by two factors: the variation of ambient factors around the OTLs, and the trade-off between modeling accuracy and computation complexity. A smaller d_v provides more accurate results but increases the computation burden, while a larger d_v reduces the accuracy of results but eases the computation burden. The transmission line segment model is applied to the improved 18-bus test system, which is derived from the IEEE 6-bus test system by adding 12 virtual nodes, as shown in Fig. 5.

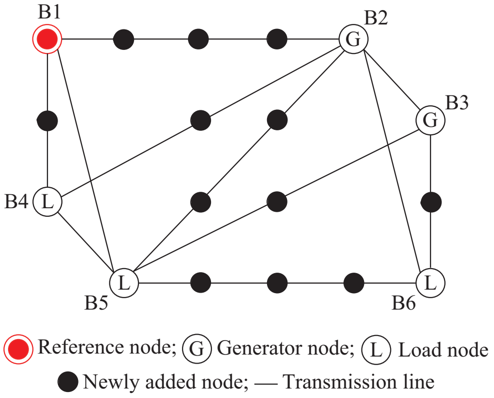

Fig. 5. Improved 18-bus test system.

The improved 18-bus test system is analyzed using both the centralized and decentralized PTL calculation methods. The base apparent power and voltage of the test system are 100 MVA and 110 kV, respectively, and the type of overhead conductor is LGL-185.

2) Rule of Changing Temporal Resolution of Ambient Data

In this paper, the time interval is set to be 15 min. However, wind direction and other ambient factors can sometimes cause significant changes over 15 min, which affect the size of convective heat dissipation Q_c and increase the computation complexity. For this case, the time scale will be adjusted to 5 min.

B. Time Evolution Curves of PTL Under Different Ambient Factors

To quantitatively express the error in the time evolution curves of PTL calculated by various methods, (58)-(60) are defined.

$$E_{\max}^{PTL}=\left|\frac{\max(\chi_{D,1\text{-}4})-\chi_T}{\chi_T}\right|\times 100\% \tag{58}$$

$$E_{\min}^{PTL}=\left|\frac{\min(\chi_{D,1\text{-}4})-\chi_T}{\chi_T}\right|\times 100\% \tag{59}$$

$$E_{range}^{PTL}=\begin{cases} E_{\max}^{PTL}+E_{\min}^{PTL} & \max(\chi_{D,1\text{-}4})\geq\chi_T \\ \left|E_{\max}^{PTL}-E_{\min}^{PTL}\right| & \max(\chi_{D,1\text{-}4})<\chi_T \end{cases} \tag{60}$$

Due to the trend similarity of time evolution curves among PTL of some regions across the four seasons, six representative regions have been selected, as shown in Fig. 6. In Fig. 6(a), the values of $E_{\max}^{PTL}$, $E_{\min}^{PTL}$, and E_{range}^{PTL} in region a are 12.77%, 6.50%, and 19.27%, respectively, which show the different PTL values for scenarios 1-4 and scenario 5. The time evolution curves of PTL for scenarios 1 and 3 are closely aligned, while there are clear differences between scenarios 2 and 4. Regions b, c, d, e, f, g, and i exhibit similar characteristics compared with region a. In Fig. 6(b), the values of $E_{\max}^{PTL}$, $E_{\min}^{PTL}$, and E_{range}^{PTL} are 9.09%, 5.07%, and 14.16%, respectively. The time evolution curves of PTL for scenarios 1-4 exhibit significant differences, and regions h, j, l, and o presents the same characteristics as region k. In Fig. 6(c), the values of $E_{\max}^{PTL}$, $E_{\min}^{PTL}$, and E_{range}^{PTL} are 8.82%, 4.99%, and 13.81%, respectively. The time evolution curves of PTL for scenarios 2 and 3 are very close, and region n exhibits the same characteristics compared with region m. Figure 6(d)-(f) shows the time evolution curves of PTL in regions p, q, and r, where the curves intersect across various scenarios, indicating less distinct separation. In Fig. 6(d), the values of $E_{\max}^{PTL}$, $E_{\min}^{PTL}$, and E_{range}^{PTL} are 1.66%, 5.85%, and 7.51%, respectively. In Fig. 6(e), the values of $E_{\max}^{PTL}$, $E_{\min}^{PTL}$, and E_{range}^{PTL} are 1.16%, 4.78%, and 5.94%, respectively. In Fig. 6(f), the values of $E_{\max}^{PTL}$, $E_{\min}^{PTL}$, and E_{range}^{PTL} are 0.7%, 7.18%, and 6.84%, respectively. The value of E_{range}^{PTL} in region q is the smallest (5.94%).

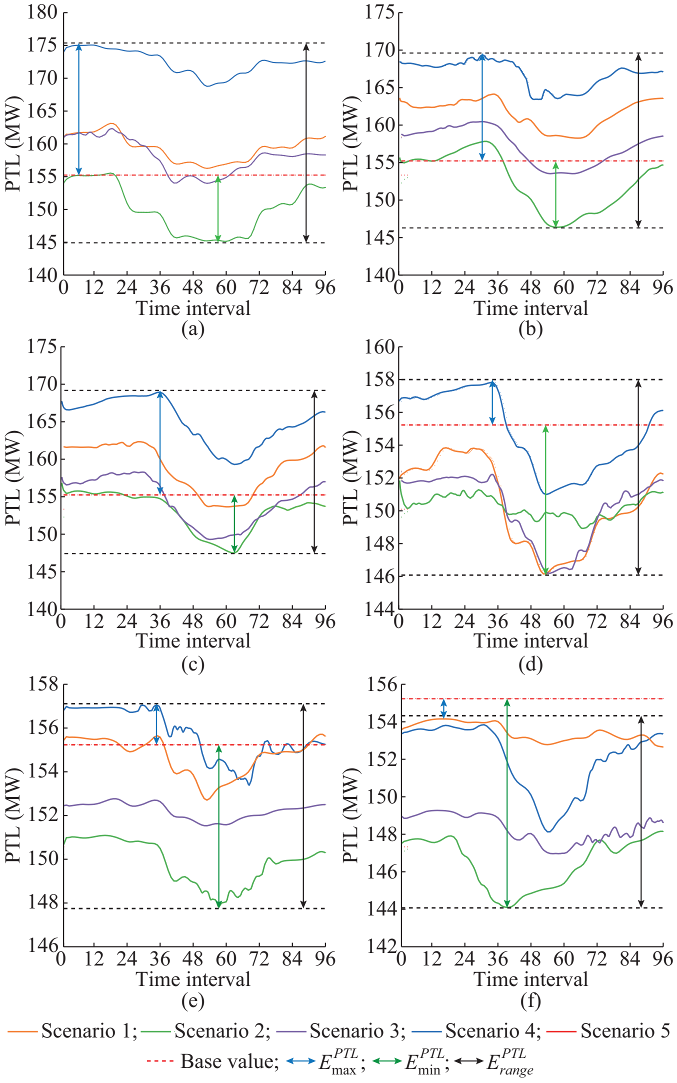

Fig. 6. Comparison of time evolution curves of PTL in various scenarios. (a) Region a. (b) Region k. (c) Region m. (d) Region p. (e) Region q. (f) Region r.

C. Analysis of Seasonal Differences in PTL

Figure 7 presents the mean, median, maximum, and minimum values of the time evolution curves of PTL across 18 regions for four scenarios. According to Fig. 7, in most regions, the minimum PTL value predominantly occurs in scenario 2, while the maximum PTL value is generally observed in scenario 4.

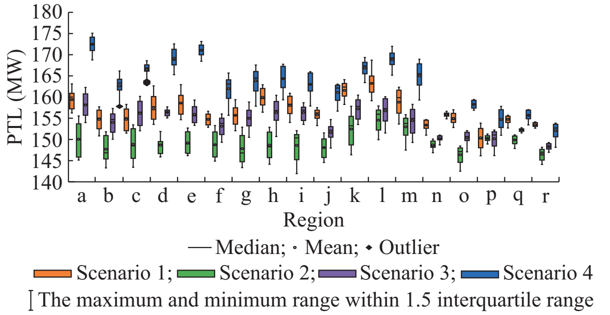

Fig. 7. Mean, median, maximum, and minimum values of time evolution curves of PTL across 18 regions.

The time evolution curves of PTL across the four scenarios present significant variation in certain regions. For example, region a exhibits the largest variation in PTL, with a range (i.e., the difference between the maximum and minimum PTL values) of approximately 29.92 MW, whereas region q shows the smallest variation, with a range of just 9.17 MW. This indicates that the impact of ambient factors on PTL varies significantly between various seasons.

D. Analysis of Spatial Differences in PTL

In this subsection, the dynamic time warping (DTW) algorithm, which compares differences between time series [37], is used to calculate the distance between the time evolution curves of PTL in various regions, referred to as *Dis*. *Dis* value closer to 1 indicates a greater difference between the time evolution curves of PTL, whereas *Dis* value closer to 0 indicates a smaller difference. The spatial difference analysis is shown in Fig. 8.

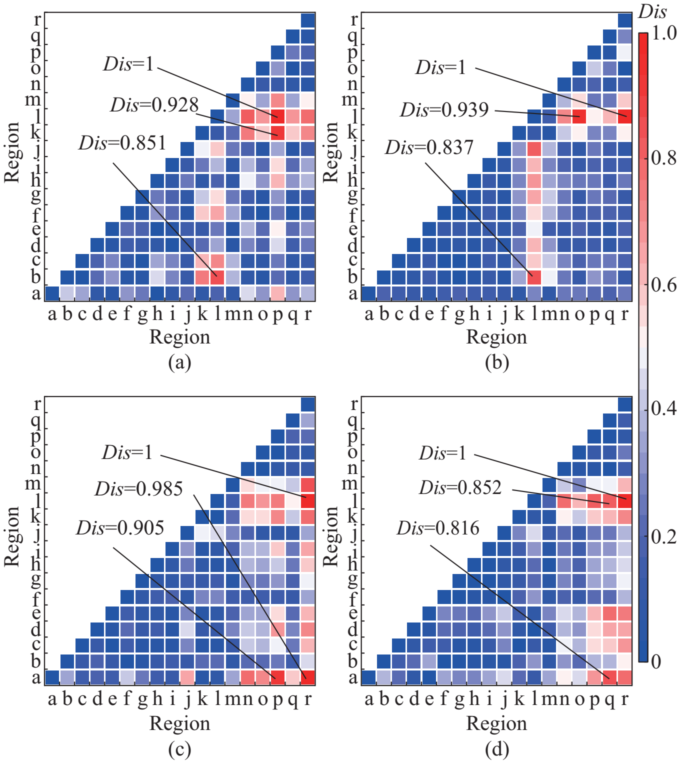

Fig. 8. Spatial difference analysis. (a) Scenario 1. (b) Scenario 2. (c) Scenario 3. (d) Scenario 4.

Figure 8 highlights the top three *Dis* values in four scenarios, revealing significant spatial differences between regions. In scenario 1, the largest difference is between regions l and p ($Dis = 1$), followed by regions p and k ($Dis = 0.928$), and regions b and p ($Dis = 0.851$). In scenarios 2, 3, and 4, regions l and r consistently show the largest difference ($Dis = 1$), with other notable pairs being q and o ($Dis = 0.939$) in scenario 2, q and r ($Dis = 0.985$) in scenario 3, and a and r ($Dis = 0.852$) in scenario 4.

E. Analysis of Method Performance

To demonstrate the performance of the proposed decentralized PTL calculation method, four methods are compared. Method 1 (M1) is the centralized PTL calculation method. Method 2 (M2) is the parallel APP method. Method 3 (M3) is the parallel ADMM method [38]. Method 4 (M4) is the proposed decentralized PTL calculation method. The computation efficiency and error between the centralized and proposed decentralized PTL calculation methods are compared to verify the convergence and effectiveness, using ambient data from four scenarios in region a. The case study is modeled in MATLAB R2020a environment on a PC equipped with an Intel$^{(R)}$ Core$^{(TM)}$ i9-10900K CPU, 3.70 GHz, 64 RAM. Equations (61) and (62) are used to quantitatively analyze β and E_r for various methods.

$$\beta = \frac{\tau_2}{\tau_1} \tag{61}$$

$$E_r = \sqrt{\frac{sum\left(\chi_{D,i} - \chi_{D,1}\right)}{N_T}} \quad i \in \{2,3,4\} \tag{62}$$

E_r and computation time are listed in Table I, with the parallel cores for M2, M3, and M4 setting to be 10.

TABLE I
COMPUTATION PERFORMANCE OF VARIOUS METHODS IN VARIOUS SCENARIOS

Method	Iteration number	E_r	Computation time (s)
M1 (scenario 1)			1868.10
M2 (scenario 1)	23	5.83×10^{-6}	320.35
M3 (scenario 1)	47	7.39×10^{-6}	531.72
M4 (scenario 1)	16	4.39×10^{-6}	215.03
M4 (scenario 2)	11	3.42×10^{-6}	137.06
M4 (scenario 3)	10	3.44×10^{-6}	108.39
M4 (scenario 4)	14	4.28×10^{-6}	156.50

As shown in Table I, M1 and M4 are almost identical. E_r in various scenarios is negligible. Compared with M2 and M3, M4 exhibits better convergence and does not need to calculate the auxiliary function. It should be noted that the computation time depends on the iteration number, and it is also influenced by the computation time of the IPM for each SP. Figure 9 shows the variation in β as the number of parallel cores increases.

As shown in Fig. 9, the computation time decreases progressively as the number of parallel cores increases, with a corresponding decrease in the value of β. This demonstrates that M4 significantly enhances computation efficiency as more parallel cores are utilized.

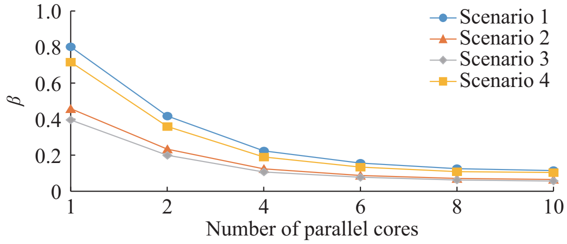

Fig. 9. Variation in β.

F. Large Test Power System

The proposed decentralized PTL calculation method is also conducted on a large test power system to test its scalability. The large test power system is based on an IEEE 39-bus test system, which consists of 39 buses, 10 generators, and 46 transmission lines. Buses 3, 4, 7, 8, 15, and 18 are set as sink buses. The detailed topology structure and system parameters can be found in [39]. Additionally, based on the transmission line segment model, 35 virtual nodes are added to the IEEE 39-bus test system to form an improved IEEE 74-bus test system, which is then used to test the proposed decentralized PTL calculation method, as shown in Fig. 10.

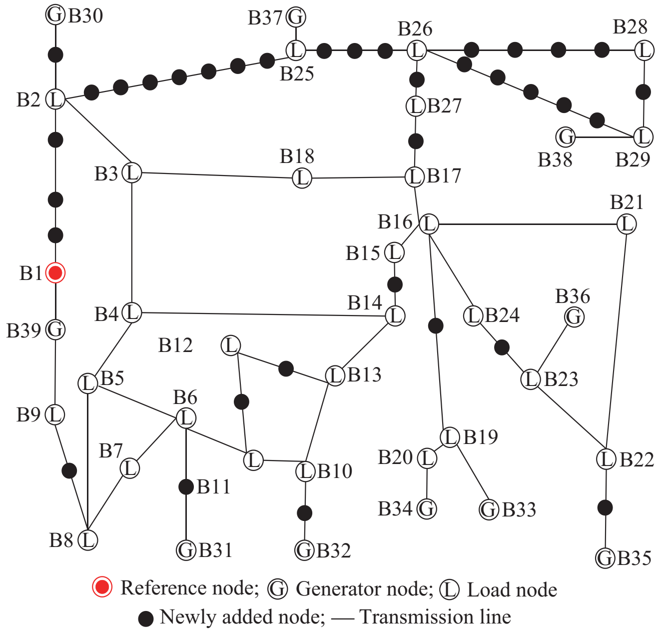

Fig. 10. Improved IEEE 74-bus test system.

In this subsection, ambient data from four scenarios in region a are selected to test the scalability of the proposed decentralized PTL calculation method. Figure 11 compares the time evolution curves of PTL in various scenarios. It can be observed that the PTL value in scenario 4 is the highest, with a maximum difference of 20.25 MW compared with that in scenario 5. In contrast, the lowest PTL value occurs in scenario 2. This demonstrates that ambient factors have a relatively significant impact on PTL values.

Table II demonstrates the test results of E_r and the computation time. It can be observed that the proposed decentralized PTL calculation method has better computation performance.

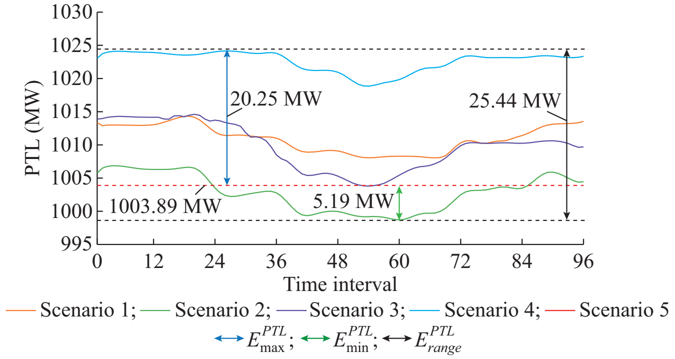

Fig. 11. Comparison of time evolution curves of PTL in various scenarios.

TABLE II
COMPUTATION PERFORMANCE UNDER VARIOUS METHODS

Method	Iteration number	E_r	Computation time (s)
M1 (scenario 1)			22557.20
M2 (scenario 1)	28	6.97×10^{-6}	2863.92
M3 (scenario 1)	86	8.23×10^{-6}	6944.12
M4 (scenario 1)	15	5.85×10^{-6}	1599.39
M4 (scenario 2)	17	4.62×10^{-6}	2146.56
M4 (scenario 3)	26	4.28×10^{-6}	1762.99
M4 (scenario 4)	17	5.14×10^{-6}	1667.84

V. CONCLUSION

For PTL calculation method, this paper proposes an improved OPF model, of which the formulations involving the ambient factors as state variables are derived. OCD is employed in the proposed decentralized PTL calculation method to reduce the complexity by converting the primal problem to multiple dimensionality reduction SPs. Case studies of different spatial-seasonal ambient factors are deployed to illustrate the marked impacts of ambient conditions that differ in space and season on PTL results. The selected area is demarcated into multiple regions, and four scenarios characterized by various seasonal features are specified as typical time frame. The data of ambient factors around OTLs corresponding to different regions or typical days are obtained from the ECMWF.

Case studies using the improved 18-bus test system based on the proposed decentralized PTL calculation method reveal that the time evolution curves of PTL exhibit significant spatial and seasonal differences due to the impact of ambient factors. In particular, the mean, median, maximum, and minimum PTL values for various seasons are compared to demonstrate the influence of ambient factors. The application of the DTW algorithm helps clarify the changing characteristics of PTL across distinct regions. Finally, the effectiveness and scalability of the proposed decentralized PTL calculation method are validated.

REFERENCES

[1] California ISO. (2022, Apr.). Summary of alert, warning, emergency, and flex alert notices issued from 1998 to 2021. [Online]. Available: http://www.caiso.com/Documents/FlexAlertNoticesIssuedFrom1998-Present.pdf

[2] J. Lu and X. Li, “Transmission expansion planning for renewable-energy-dominated power grids considering climate impact,” *Journal of Modern Power Systems and Clean Energy*, vol. 12, no. 6, pp. 1737-1748, Nov. 2024.

[3] D. Xu, Z. Cai, Q. Cheng*et al*., “Security-constrained transmission maintenance optimization considering generation and operational risk costs,” *Journal of Modern Power Systems and Clean Energy*, vol. 12, no. 3, pp. 767-781, May 2024.

[4] California ISO. (2020, Qct.). CAISO, CPUC, and CEC issue preliminary report on causes of august rotating outages. [Online]. Available: https://www.caiso.com/Documents/CAISO-CPUC-CEC-Issue-Preliminary-Report-Causes-August-Rotating-Outages.pdf

[5] California ISO. (2020, Sept.). Grid avoids calling for outages with help from conservation, says ISO. [Online]. Available: https://www.flexalert.org/news/97-grid-avoids-calling-for-outages-with-help-from-conservation

[6] X. Dong, C. Wang, J. Liang *et al*., “Calculation of power transfer limit considering electro-thermal coupling of overhead transmission line,” *IEEE Transactions on Power Systems*, vol. 29, no. 4, pp. 1503-1511, Jul. 2014.

[7] C. S. Indulkar, B. Viswanathan, and S. S. Venkata, “Maximum power transfer limited by voltage stability in series and shunt compensated schemes for AC transmission systems,” *IEEE Transactions on Power Delivery*, vol. 4, no. 2, pp. 1246-1252, Apr. 1989.

[8] Y. Xiao, Y. Song, and Y. Sun, “A hybrid stochastic approach to available transfer capability evaluation,” *IEE Proceedings – Generation, Transmission and Distribution*, vol. 148, no. 5, pp. 420-426, Oct. 2001.

[9] M. M. Othman, M. Fotuhi-Firuzabad, N. A. Salim *et al*., “Determination of available transfer capability with implication of cascading collapse uncertainty,” *IET Generation Transmission & Distribution*, vol. 8, no. 4, pp. 705-715, Apr. 2014.

[10] A. B. Rodrigues and M. G. D. Silva, “Probabilistic assessment of available transfer capability based on Monte Carlo method with sequential simulation,” *IEEE Transactions on Power Systems*, vol. 22, no. 1, pp. 484-492, Feb. 2007.

[11] Y. Huang, T. Ding, P. Wang *et al*., “Linearized AC power flow model-based interval total transfer capability evaluation with uncertain renewable energy integration,” *International Journal of Electrical Power & Energy Systems*, vol. 154, pp. 1-9, Dec. 2023.

[12] X. Wang, X. Wang, H. Sheng *et al*., “A data-driven sparse polynomial chaos expansion method to assess probabilistic total transfer capability for power systems with renewables,” *IEEE Transactions on Power Systems*, vol. 36, no. 3, pp. 2573-2583, May 2021.

[13] H. Chen, X. Fang, R. Zhang *et al*., “Available transfer capability evaluation in a deregulated electricity market considering correlated wind power,” *IET Generation Transmission & Distribution*, vol. 12, no. 1, pp. 53-61, Nov. 2017.

[14] X. Kou and F. Li, “Interval optimization for available transfer capability evaluation considering wind power uncertainty,” *IEEE Transactions on Sustainable Energy*, vol. 11, no. 1, pp. 250-259, Jan. 2020.

[15] X. Dong, X. Hao, M. Wang *et al*., “Power transfer limit calculation for multi-area interconnected power networks,” *International Journal of Electrical Power & Energy Systems*, vol. 120, no. 2020, pp. 1-9, Sept. 2020.

[16] X. Dong, X. Hao, Q. Chen *et al*., “A distributed power transfer limit calculation method for multi-area interconnection power networks,” *IEEE Transactions on Power Systems*, vol. 36, no. 5, pp. 4723-4732, Sept. 2021.

[17] X. Jia, X. Dong, B. Xu *et al*., “Static voltage stability assessment considering impacts of ambient conditions on overhead transmission lines,” *IEEE Transactions on Industry Applications*, vol. 58, no. 6, pp. 6981-6989, Nov. 2022.

[18] J. Cao, W. Du, and H. Wang, “Weather-based optimal power flow with wind farms integration,” *IEEE Transactions on Power Systems*, vol. 31, no. 4, pp. 3073-3081, Jul. 2015.

[19] Y. Li, Y. Wang, and Q. Chen, “Study on the impacts of meteorological factors on distributed photovoltaic accommodation considering dynamic line parameters,” *Applied Energy*, vol. 259, pp. 1-10, Feb. 2020.

[20] M. Nick, O. Alizadeh-Mousavi, R. Cherkaoui *et al*., “Security constrained unit commitment with dynamic thermal line rating,” *IEEE Transactions on Power Systems*, vol. 31, no. 3, pp. 2014-2025, May 2016.

[21] Y. Wang, Y. Wang, X. Dong *et al*., “Capacity assessment for wind-storage integration system considering electro-thermal coupling of overhead transmission line,” *IEEE Transactions on Power Systems*, vol. 39, no. 1, pp. 967-975, Jan. 2024.

[22] X. Dong, C. Kang, H. Sun *et al*., “Analysis of power transfer limit

considering thermal balance of overhead conductor," *IET Generation Transmission & Distribution*, vol. 9, no. 14, pp. 2007-2013, Nov. 2015.

[23] S. Madadi, B. Mohammadi-Ivatloo, and S. Tohidi, "Probabilistic available transfer capability evaluation considering dynamic line rating based on a sequential game-theoretic approach," *IEEE Systems Journal*, vol. 16, no. 1, pp. 891-901, Mar. 2022.

[24] Z. Zhang and Y. Ju, "An embedded consensus ADMM distribution algorithm based on outer approximation for improved robust state estimation of networked microgrids," *Journal of Modern Power Systems and Clean Energy*, vol. 12, no. 4, pp. 1217-1226, Jul. 2024.

[25] Z. Zhang, C. Wang, Q. Wu *et al*., "Optimal dispatch for cross-regional integrated energy system with renewable energy uncertainties: a unified spatial-temporal cooperative framework," *Energy*, vol. 292, pp. 130433, Apr. 2024.

[26] N. F. Avila and C. Chu, "Distributed probabilistic ATC assessment by optimality conditions decomposition and LHS considering intermittent wind power generation," *IEEE Transactions on Sustainable Energy*, vol. 10, no. 1, pp. 375-385, Jan. 2019.

[27] A. Rabiee, B. Mohammadi-Ivatloo, and M. Moradi-Dalvand, "Fast dynamic economic power dispatch problems solution via optimality condition decomposition," *IEEE Transactions on Power Systems*, vol. 29, no. 2, pp. 982-983, Mar. 2014.

[28] T. H. Kim, H. Shin, K. Kwag *et al*., "A parallel multi-period optimal scheduling algorithm in microgrids with energy storage systems using decomposed inter-temporal constraints," *Energy*, vol. 202, pp. 1-14, Jul. 2020.

[29] *IEEE Standard for Calculating the Current-temperature Relationship of Bare Overhead Conductors*, IEEE Standard 738-2012, 2012.

[30] A. J. Conejo, F. J. Nogales, and F. J. Prieto, "A decomposition procedure based on approximate Newton directions," *Mathematical Programming*, vol. 93, pp. 495-515, Dec. 2002.

[31] X. Jia, H. Sun, Y. Ma *et al*., "Calculation of available transmission capacity of power grid considering the influence of environmental factors," in *Proceedings of 2022 IEEE 6th Information Technology and Mechatronics Engineering Conference (ITOEC)*, Chongqing, China, Mar. 2022, pp. 1843-1847.

[32] H. Hersbach, B. Bell, P. Berrisford *et al*. (2018, Jan.). ERA5 hourly data on single levels from 1979 to present. [Online]. Available: https://cds.climate.copernicus.eu/datasets2018

[33] X. Jia, X. Dong, H. Sun *et al*., "Calculation of power grid transmission characteristics and sensitivity analysis considering meteorological and geographic factors," *Automation of Electric Power Systems*, vol. 46, no. 21, pp. 106-115, Jan. 2022.

[34] X. Jia, Q. Niu, M. Chen *et al*., "Analysis of power flow characteristics of power grid considering temporal and spatial correlation of meteorological factors," in *Proceedings of 2021 IEEE/IAS Industrial and Commercial Power System Asia (I&CPS Asia)*, Chengdu, China, Jul. 2021, pp. 758-764.

[35] V. Cecchi, M. Knudson, and K. Miu, "System impacts of temperature-dependent transmission line models," *IEEE Transactions on Power Delivery*, vol. 28, no. 4, pp. 2300-2308, Oct. 2013.

[36] C. Valentina and S. L. A. M. Karen, "Incorporating temperature variations into transmission-line models," *IEEE Transactions on Power Delivery*, vol. 26, no. 4, pp. 2189-2196, Oct. 2011.

[37] G. Pan, Z. Gu, Y. Sun *et al*., "Multi-stage provincial power expansion planning and multi-market trading equilibrium," *Journal of Modern Power Systems and Clean Energy*, vol. 12, no. 5, pp. 1652-1665, Sept. 2024.

[38] W. Deng, M. Lai, Z. Peng *et al*., "Parallel multi-block ADMM with O (1/k) convergence," *Journal of Scientific Computing*, vol. 71, pp. 712-736, Nov. 2016.

[39] Illinois Center for a Smarter Electric Grid. (2024, Nov.). Literature-based power flow test cases: IEEE 39-bus system. [Online]. Available: https://icseg.iti.illinois.edu/ieee-39-bus-system/

Xueyong Jia received the B.S. degree in electrical engineering and automation from North China University of Science and Technology, Tangshan, China, in 2020 and the M.S. degree in electrical engineering from Shandong University, Jinan, China, in 2023. His research interests include power system analysis and operation.

Xiaoming Dong received the B.S., M.S., and Ph.D. degrees in electrical engineering from the School of Electrical Engineering, Shandong University, Jinan, China, in 2003, 2009, and 2013, respectively. He is currently an Associate Professor with Shandong University. His research interests include power system stability, operation, and control.

Chengfu Wang received the B. S. degree from Northeast Electric Power University, Jilin, China, in 2006, the M. S. degree from Harbin Institute of Technology, Harbin, in 2008, and the Ph. D. degree in electrical engineering from the School of Electrical Engineering, Shandong University, Jinan, China, in 2012. He is currently an Associate Professor with Shandong University. His research interests include planning and operation of wind power system, active distribution system, and integrated energy system.

Ming Yang received the B. E. and Ph. D. degrees in electrical engineering from Shandong University, Jinan, China, in 2003 and 2009, respectively. From 2006 to 2007, he was an exchange Ph.D. Student with Energy System Research Center, University of Texas at Arlington, Arlington, USA. From 2009 to 2011, he conducted Postdoctoral Research with the School of Mathematics, Shandong University. From 2015 to 2016, he was a Visiting Scholar with the Energy Systems Division, Argonne National Laboratory, Argonne, USA. He is currently a Professor with Shandong University. His research interests include power system optimal operation and control.

Tianguang Lu received the B.S. degree in electrical engineering from Shandong University, Jinan, China, in 2013, the M. S. degree in Computer Science from Georgia Institute of Technology, Atlanta, USA, and the Ph.D. degree in electrical engineering from Shanghai Jiao Tong University, Shanghai, China, in 2018. He is currently a Professor with Shandong University and an Associate Professor with Harvard University, Cambridge, USA. His research interests include optimization for low-carbon power systems and interaction between energy system and atmosphere.